Editors' Choice—4D Neutron and X-ray Tomography Studies of High Energy Density Primary Batteries: Part I. Dynamic Studies of LiSOCl2 During Discharge

Editors' Choice—4D Neutron and X-ray Tomography Studies of High Energy Density Primary Batteries: Part I. Dynamic Studies of LiSOCl2 During Discharge

SCHOLARONE™
Manuscripts

1 **Editors' Choice—4D Neutron and X-ray Tomography Studies of High Energy**

2 **Density Primary Batteries: Part I. Dynamic Studies of LiSOCl₂ during**

3 **Discharge**

4

5

6 Ralf F. Ziesche,[1,2,3,4] James B. Robinson,[1,2] Matthew Kok,[1,2] Henning Markötter,[5,6,7] Winfried

7 Kockelmann,[4] Nikolay Kardjilov,[5] Ingo Manke,[5] Dan J. L. Brett,[1,2] and Paul R. Shearing[1,2,z]

8 [1]Electrochemical Innovation Lab, Department of Chemical Engineering, UCL, London, WC1E 7JE, UK

9 [2]The Faraday Institution, Quad One, Harwell Science and Innovation Campus, Didcot, OX11 0RA, UK

10 [3]Diamond Light Source Ltd, Harwell Science and Innovation Campus, Didcot, OX 11 0DE, UK

11 [4]STFC, Rutherford Appleton Laboratory, ISIS Facility, Harwell, OX11 0QX, UK

12 [5]Helmholtz-Zentrum Berlin für Materialien und Energie (HZB), , 14109 Berlin, Germany

13 [6]Technische Universität Berlin,   10624 Berlin, Germany

14 [7]Bundesanstalt für Materialforschung und -Prüfung,   12205 Berlin, Germany

15

16 [z]E-mail: p.shearing@ucl.ac.uk

17

Abstract

19 The understanding of dynamic processes in Li-metal batteries is an important consideration to

20 enable the full capacity of cells to be utilised. These processes, however, are generally not

21 directly observable using X-ray techniques due to the low attenuation of Li; and are challenging

22 to visualise using neutron imaging due to the low temporal resolution of the technique. In this

23 work, complementary X-ray and neutron imaging are combined to track the dynamics of Li

24 within a primary Li/SOCl₂ cell. The temporal challenges posed by neutron imaging are

25 overcome using the golden ratio imaging method which enables the identification of Li

26 diffusion *in operando*. This combination of techniques has enabled an improved understanding

27 of the processes which limit rate performance in Li/SOCl₂ cells and may be applied beyond

28 this chemistry to other Li-metal cells.

29

Introduction

31 Lithium batteries have transformed energy storage technology due to their significant

32 advantages in comparison to other cell chemistries, including their high cell voltage,

33 comparatively lightweight nature of the cells, long cycle life and high capacity and rate

34 performance. These characteristics have enabled Li cells to be deployed in applications as

35 varied as portable electrical devices, medical implants [1], automotive powertrains [2] or for

36 applications in space [3]. Primary Li cells have historically been preferred for long-duration

37 backup power due to their outstanding shelf-life, high potential and capacity. One of the most

38 common cell chemistries for such applications is the Li metal vs. thionyl chloride (SOCl₂) [4–

39 7] cell which is also suitable for applications under extreme conditions including very low or

40 high temperatures [8,9]. Li-SOCl$_2$ primary batteries are mainly available in two cell designs:

41 the bobbin configuration, investigated in that manuscript, and as a spirally wound cell. Bobbin

42 type cells, while low cost and relatively simple to manufacture, can show a fundamental

43 capacity loss at higher discharge rates. A number of different factors can prematurely interrupt

44 the cell operation, such as the loss of the electrical or ionic conductivity of the electrodes. An

45 improved understanding of mechanisms which lower the cell capacity and lifetime is crucial

46 for designing improved batteries.

47 Three-dimensional (3D) and four-dimensional (4D) imaging, i.e. 3D spatially and temporally

48 resolved methods such as X-ray computed tomography (CT), are powerful tools to track

49 processes which affect battery performance. The high spatial and time resolution which range

50 from the millimetre to the nanometre length scale [10], exposure times of fractions of a second

51 to acquire radiographic images [11,12] and as little as several seconds for full CTs [13–15]

52 enable the study of the battery architecture, electrode microstructure, new battery materials and

53 battery safety. The high sensitivity to high-Z elements provides a good imaging contrast for

54 metallic materials such as the anode and cathode current collectors, and the active electrode

55 materials such as LiMnO$_2$ [15], LCO [16], LFP [17] or NMC [18]. However, light elements

56 such as lithium appear transparent when imaged with X-rays, in the 'tender' or hard X-ray

57 energy spectrum. In contrast, neutrons show a high sensitivity for some low-Z elements

58 providing a high contrast for both lithium and hydrogen. In contrast, some metals such as lead

59 have low attenuation coefficients when imaged using neutrons. This is a consequence of X-

60 rays interacting with the electron cloud with the attenuation coefficient increasing with a rising

61 Z, whereas neutrons interact with the nucleus and provide different attenuation coefficients

62 even between isotopes of the same element. Recently, neutron tomography has demonstrated

63 significant potential in imaging electrochemical devices, for example, for visualising the water

64 evolution in fuel cells [19–21] and electrolysers [22,23], to examine dynamic Li diffusion

65 processes and electrode expansion [24–27], electrolyte consumption [28] and gas evolution

66 [29–31] in Li batteries. However, neutron imaging is often limited to radiography and suffers

67 from poor spatial resolution and long exposure times due to the characteristically low flux

68 available at most neutron sources. This makes it challenging to image dynamic processes at

69 high-resolution. Recent developments have shown an improved speed in neutron CT collection

70 [32,33] and spatial resolutions down to a few micrometres [34–36] are achievable, which in

71 turn has increased the potential to track dynamic lithium diffusion processes in lithium batteries.

72 In cases where dynamic processes are slow, neutron sources with a lower flux can perform 4D

73 studies by using an appropriate spatiotemporal scanning strategy, such as the golden-ratio (GR)

74 scanning method. Conventional tomographic reconstruction techniques require projections in

75 sequences of equal angular distances. The spatial and temporal resolution is predetermined and

76 cannot be changed during the measurements or afterwards. Additionally, if one of the
77 sequential projections is missing or defective, caused by problems with the camera system or
78 an interruption of the radiation, the data cannot be reconstructed or will contain significant
79 artefacts. In the case of a static sample the missing projections can be repeated, or fluctuations
80 of the neutron flux can be monitored and balanced by the variation of the exposure time.
81 However, replacing lost projections is not possible for dynamic processes. The mathematical
82 background and a demonstration of the GR technique is shown by Kaestner *et al.* [37]. This
83 scanning strategy is based on non-sequential decompositions of the sample rotation angle
84 sequence. The organisation of the projections by using the golden-ratio was first introduced by
85 Köhler [38], who organised the projections by using the GR (shown in Equation 1) to calculate
86 the optimal acquisition angle of each projection such as shown in Equation 2 for a tomographic
87 scan over 180° with n the number of the projections.

$$g = \frac{\sqrt{5} - 1}{2} \approx 0.618 \qquad \text{Equation 1}$$

$$GR \ angle \ (n) = g \cdot n \cdot 180\,° \ mod \ 180\,° \ |n \ \epsilon \ \mathbb{Z}_0^+ \qquad \text{Equation 2}$$

88 The next angle is centred in the biggest gap of the previously acquired angles to minimise the
89 overlap of the completed projections and prevent redundant information. Using this method, a
90 time-resolved data set is achieved by using a certain set of consecutive projections, possibly
91 with a high overlap of the projections between consecutive tomographies in a running-average
92 mode. For an improvement in spatial resolution, a larger number of consecutive projections is
93 used and the projection overlap can be reduced.

94 The combination of both non-destructive neutron and X-ray CT techniques provides
95 opportunities to combine structural information such as particle movements, obtained from the
96 X-rays, with electrochemical information such as lithium diffusion or the lithium content
97 change in the cathode or anode, obtained from the neutrons. The successful combination of X-
98 ray and neutron CT on batteries was for the first time demonstrated by LaManna et al. [39].
99 This combination of complementary imaging techniques enables the study of the dynamic
100 processes inside batteries in 4D and provides opportunities to deliver new insights in processes
101 which occur simultaneously such as e.g. Li diffusion and electrode expansion [40].

102

103 **Experimental**

104 1200 mAh LS 14250 Li-SOCl$_2$ cells (Saft Groupe A.A., France) were examined to understand
105 the rate-dependent structural changes using a combination of X-ray and neutron imaging. The
106 LS 14250 cell is a ½ AA sized commercial Li/SOCl$_2$ battery with an internal bobbin type
107 structure designed for low-rate applications such as backup batteries in computers or burglar
108 alarm systems. This low-cost, primary cell type provides a nominal voltage of 3.6 V at room

109   temperature with a flat discharge profile over a long-time range and can operate over a wide

110   temperature range of –60−85 °C, with a very low self-discharge rate, which makes the cell

111   chemistry a popular choice for applications in extreme conditions [5,41]. Figure 1(a) shows the

112   schematic drawing of the internal structure of a bobbin type Li/$SOCl_2$ battery cell. The liquid

113   $SOCl_2$ cathode (green) in the middle of the cell is surrounded by the lithium-metal negative

114   electrode (grey) and separated by a separator layer (yellow) soaked in a $SOCl_2$:$LiAlCl_4$ non-

115   aqueous electrolyte (blue). A porous supporting carbon skeleton surrounds the liquid cathode

116   providing an enhanced electrical conductivity. A cathode current collector rod (grey) in the

117   centre of the cell connects this porous carbon to the positive tab. The lithium anode is directly

118   connected to the cell can which acts as the negative terminal. During cell discharge Li-ions

119   move from the Li anode into the electrolyte, diffuse through the Li^+ permeable separator layer

120   to the cathode side and react with the $SOCl_2$ to form LiCl, SO_2 gas and solid sulphur.

121   Two LS 14250 cells were discharged under constant current conditions at 25 mA and 8 mA,

122   respectively. Both of these discharge currents are below the maximum recommended discharge

123   current of 35 mA, however, these rates are known to result in a significant loss of usable

124   capacity, as detailed in the cell data sheet.
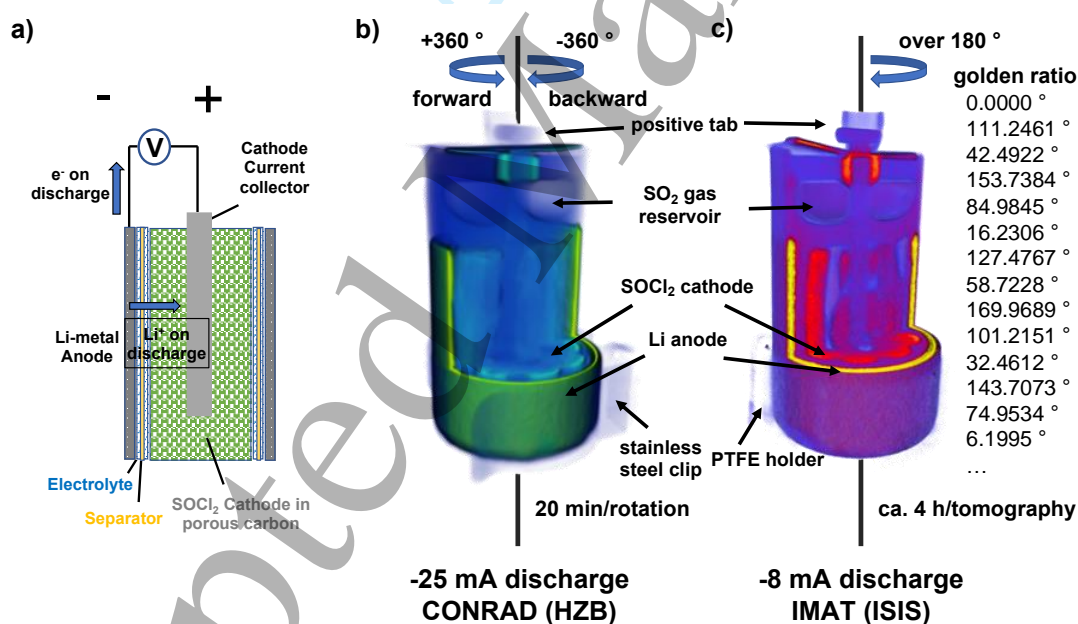
125

126   **Figure 1 (a) schematic illustration of a Li-metal/thionyl chloride bobbin type cell (b) 3D reconstruction of a LS14250 cell discharged**

127   **at 25 mA while being scanned on the CONRAD-2 neutron imaging beamline with sequences of equal angular projections in forward**

128   **and backward rotation through 360° and (c) 3D reconstructions of a LS14250 cell discharged at 8 mA scanned on the IMAT beamline**

129   **with the GR decomposition strategy. The first projection angles for the GR scan are listed on the right hand side.**

130   Time resolved neutron CT scans at a 25 mA discharge current were performed at the V7

131   CONRAD-2 neutron imaging beamline [42,43] at the BER II research reactor at the Helmholtz

132   Zentrum Berlin. CONRAD-2 is optimised for high spatial and time resolved neutron imaging.

133 The intermediate measuring position of CONRAD-2 was used to maximize the high neutron

134 flux at an acceptable spatial resolution. This position was equipped with a high speed, indirect

135 detector system including a 200 µm thick ^{6}LiF/ZnS:Ag scintillator screen for a high neutron to

136 light conversion efficiency and a cooled -30 °C sCMOS 'Neo' camera from Oxford

137 Instruments/Andor (UK) which provides a high frame rate with short readout delays. Both

138 components were used in combination with a bright Nikon photo lens (f =50 mm, aperture 1.2)

139 to reduce the light losses inside the camera box and focus the object on to the camera photo

140 chip. For an optimal L/D ratio a 3 cm pinhole configuration was selected, positioned about 5 m

141 in the front of the detector system at the end of the NL-1B neutron guide. The LS 14250 cell

142 was mounted in front of the scintillator screen on an adjustable stick on the V7 rotation stage

143 (Goniometer 409, Huber Diffraktiontechnik, Germany) by a stainless steel clip. With a

144 calculated L/D of about 167, the spatial resolution was about 150 µm with a pixel size of 55 µm.

145 Before the cell was secured onto the sample holder the plastic coating was removed to mitigate

146 the contribution of this layer to neutron scattering. The electrical connection to the GAMRY

147 1000E potentiostat (GAMRY Instruments, USA) was maintained by a stainless steel clip at the

148 electrical negative cell can and a crocodile clip at the top positive terminal tab. The battery was

149 discharged in constant current mode at 25 mA. During discharging, continuous neutron

150 radiographies were collected with an exposure time of 2 s per image by the Andor Solis

151 software. Tomograms were sequentially accumulated during 360° rotation with 600 projections

152 acquired for each full tomography in approximately 20 mins. Every hour, two tomographies

153 were performed whereby the first was acquired through a counter-clockwise rotation and the

154 second clockwise; labelled as forward and backward respectively. Figure 1(b) shows an

155 example of a 3D data set with an illustration of the rotation conditions. After every second

156 tomography, the battery was translated out of the beam to collect open beam and dark field

157 images to enable the correction and normalisation of the projections. For data processing the

158 'Remove Outliers' and median filter of ImageJ Fiji [44] were used to remove white spots which

159 are caused by fast neutrons and gamma radiation from the 16-bit images. Reconstruction of the

160 tomographies was performed using the Octopus 8.9 software (XRE, Gent, Belgium) using the

161 filtered back projection (FBP) reconstruction algorithm. Due to the high neutron absorption of

162 lithium, the reconstructed slices were then corrected for beam hardening using the first

163 tomogram to determine the parameters which are utilised for all following tomograms. The

164 parameters are optimised in such a way that the lithium anode and the $SOCl_2$ cathode, in the

165 middle of the cell, show a homogeneous attenuation coefficient respectively. Throughout the

166 experiment 47 full tomograms were collected, 24 in forward and 23 in backward rotation with

167 the process taking ca. 20.3 h and the battery providing a capacity of 506 mAh.

168 A second 4D neutron imaging scan with an 8 mA discharge current was performed on the IMAT

169 neutron imaging beamline [45–47] at the ISIS neutron spallation source. In contrast to most

170   reactor based neutron sources, neutron spallation sources such as the ISIS neutron source at the

171   Rutherford Appleton Laboratory (UK) have a lower time-averaged neutron flux which makes

172   imaging of dynamic processes with the conventional scanning strategies more difficult. To

173   overcome this challenge, methods such as the Golden Ratio (GR) strategy can be employed.

174   Using this method, the sample is imaged at non-regular intervals with the organisation of the

175   angular distribution calculated by the GR. This method can be used for angular ranges of π or

176   2π with each consecutive scanning angle minimising the overlap of the previously scanned

177   projections avoiding the acquisition of redundant information. GR projections are acquired

178   continuously, over a chosen experimental period, enabling the optimisation of either the

179   temporal or spatial resolution by post-image processing by selecting the number of projections

180   from the GR tomogram that are reconstructed. By ensuring an overlap of the projections of

181   consecutive tomographies in the projection sequence (i.e. taking a 'running average') an

182   improved time resolution is achieved. As the neutron flux at the ISIS spallation source is

183   approximately $10\times$ lower than at CONRAD-2 for the same L/D ratio, the GR decomposition

184   strategy was applied here. An indirect detector box with a 80 µm thick ^{6}LiF/ZnS:(Cu/Ag)

185   scintillator (Tritec, Switzerland) in combination with a Nikon photo lens (f =135 mm, aperture

186   2) and an ANDOR Zyla sCMOS 4.2 PLUS camera (Oxford Instruments Andor, UK) was

187   utilised. The box was adjusted to a pixel size of 29 µm with a pinhole size of 40 mm with a

188   L/D ratio of ca. 250 which achieved a spatial resolution of about 80 µm. Once more, the plastic

189   cover of the LS 14250 battery cell was removed, before the cell was inserted in a neutron

190   transparent cylindrical PTFE sample holder. Electrical connections were maintained by

191   attaching a copper cable between the negative battery can and the PTFE wall and attaching a

192   crocodile clip to the positive battery tab. The PTFE holder was screwed to an adapter rod which

193   was mounted onto a Huber Goniometer 411 (HUBER Diffraktionstechnik, Germany) rotation

194   stage and positioned close to the camera box. Due to the limited rotation angle between 0° and

195   180° no specialised cable connection such as a slip ring was needed. Owing to the low neutron

196   flux, a long exposure time of 30 s was used to maximise counting statistics. A GAMRY 1000E

197   potentiostat discharged the cell at a constant current mode of 8 mA during the scan. The angular

198   distribution for the whole scan was calculated using the GR with Figure 1(c) showing a 3D

199   reconstruction of the partially discharged cell and the first calculated GR projection angles over

200   an angular range of π. In advance of the discharge scan of the cell, a 4 h tomography was

201   acquired to enable a full reconstruction of the cell in pristine condition. After every 610

202   projections the cell was moved out of the beam for five open beam images to facilitate image

203   correction after all the projections had been acquired. The total discharging process took about

204   104 h, after which the cell had delivered a capacity of 832 mAh. After correcting each

205   projection using the dark and open beam images, and after filtering white spots, 3D

206   reconstructions were performed *via* the FBP algorithm for a parallel beam using the ASTRA

207 toolbox [48,49] reconstruction library within the python programming language. For the

208 number of projections, the Fibonacci number 377 was utilised due to a better reconstruction

209 result in combination with a shift of 188 projections for each following reconstruction. This

210 results in an overlap of 189 projections and a time shift of about 2 h between the tomographies.

211 Four dimensional X-ray tomography was achieved on a Nikon XTH 225 laboratory X-ray

212 system (Nikon Corporation, Japan) using a 225 kV reflection target source with a focal spot

213 size of 3 µm at 7 W. A PerkinElmer 1620 16-bit (PerkinElmer Inc. USA) detector with a

214 2000×2000 pixel array and a pixel size of 200 µm was used to capture all images. The plastic

215 cover of the cell was removed prior to mounting the cell with double-sided tape onto the sample

216 holder of the rotation stage. An electrical connection was maintained by applying a crocodile

217 clip to the positive tab, with the negative connection achieved by connecting a copper cable to

218 the cell can using insulating tape. Both cables were then connected to an electrical slip ring (P4

219 + Compact Slip Ring, Moog, UK) which allowed a continuous rotation of the stage without

220 losing the electrical connection. The battery was discharged using a GAMRY 1000E

221 potentiostat (GAMRY Instruments, USA) in constant current mode with a discharge current of

222 25 mA. The instrument was programmed to continuously collect projections at an X-ray tube

223 voltage level of 120 kV and current of 140 µA. To achieve one full tomogram, 1201 projections

224 were captured through an angular range of 360° with an exposure time of 1 s per projection,

225 leading to a total image acquisition time of ca. 20 mins. The total cell discharge took about

226 18.3 h and reached a capacity of 459 mAh which enabled the capture of 56 full tomographies

227 of the cell during discharge. The tomograms were reconstructed using the FDK (FDK_CUDA)

228 circular cone beam reconstruction algorithm from the ASTRA toolbox [48,49] reconstruction

229 library within the python programming language. Before starting the 3D reconstruction, the

230 projections were corrected by the dark field and open beam images which were collected before

231 and after the scan and binned by a factor of two to reduce the reconstruction time and data size

232 resulting in a reconstructed pixel size of 40.4 µm.

233

234 **Results and Discussion**

235 As shown in Figure 2(a) the discharge curves of all three discharged LS 14250 cells show the

236 typical flat discharge profiles at a high potential expected for the Li/SOCl$_2$ chemistry. The cells

237 operated at the higher discharge current of 25 mA display a lower potential plateau at ca. 3.3 V

238 with the cell discharged at 8 mA exhibiting a slightly higher potential plateau in excess of 3.4 V.

239 At the beginning of the discharging process, the voltage delay, characteristic of Li/SOCl$_2$ cells,

240 can be seen to be shorter for the cell discharged at a higher current requiring ca. 0.5 h before

241 the potential is stabilised [Figure 2(c)]. In comparison, a long delay of about 30 h is observed

242 for the low current discharge in Figure 2(a). This initial voltage delay occurs in Li/SOCl$_2$ cells

243 due to the formation of a passivating LiCl layer at the anode during cell storage. The increased
244 time needed to recover the normal potential of the cell observed during the low discharge is
245 due to a reduced level of mechanical disruption, which removes the passivation layer on the
246 lithium metal surface [50]. At the point the voltage recovers to a plateaued voltage the whole
247 Li-metal surface can participate in the discharge reaction. The slightly lower potential of the
248 cell scanned with X-ray compared to the one scanned with neutrons is attributed to
249 manufacturing variations. The difference in cell capacity of 459 mAh compared to 506 mAh
250 may be a result of a higher self-discharge during a longer cell storage time, or differences in
251 the active mass loading during manufacture. Internal mechanisms in the cell such as the
252 shielding of active electrode material by a SO_2 gas layer on the Li-metal surface can result in
253 similar effects.
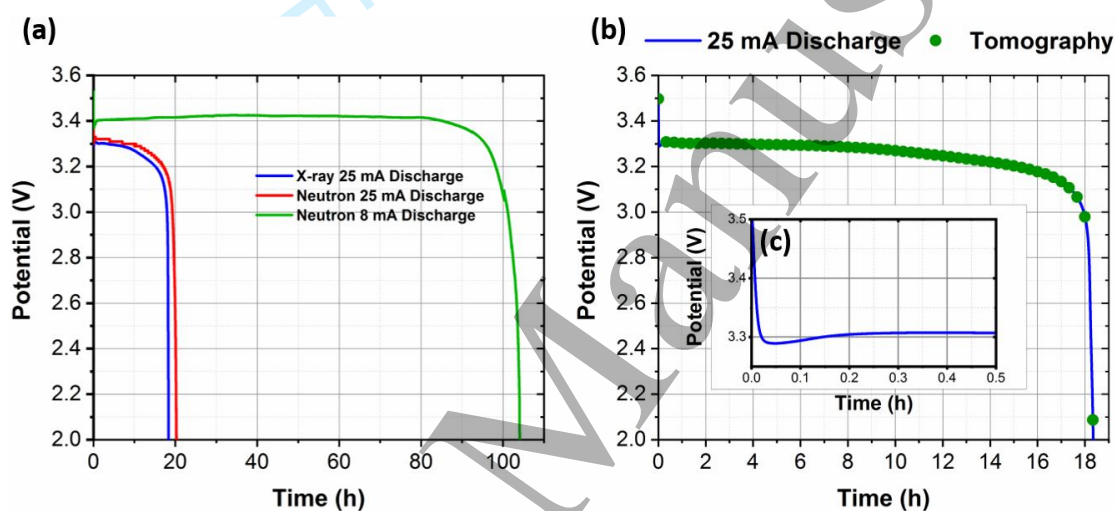
254

255 **Figure 2 (a) Discharge curves of the three LS14250 cells used in this work, two discharged at 25 mA scanned with X-rays and neutrons**
256 **and one cell at 8 mA imaged with neutrons (b) A detailed discharge curve of the cell discharged at 25 mA scanned with X-rays. Green**
257 **dots mark the times when tomograms were recorded. (c) a magnified view of the voltage delay at the beginning of the cell discharging**
258 **process, typical for Li/SOCl$_2$ chemistry.**

259 Laboratory X-ray scanners or synchrotron imaging beamlines in the intermediate or lower hard
260 X-ray energy regime show lithium metal or lithium diffusion in a lithium battery cell only
261 indirectly by a grey value increase in the electrode, where the lithium is removed and a grey
262 value reduction where lithium is deposited. This behaviour is visible for the LS 14250 cell
263 scanned with X-rays in Figure 3, which shows horizontal and vertical slices of the pristine, half
264 discharged and fully discharged cell. The metallic battery components such as the positive tab,
265 the negative cell can and the cathode current collector are clearly visible, with the battery
266 header somewhat obscured due to reconstruction artefacts. Furthermore, the liquid $SOCl_2$
267 cathode in the middle of the cell can be seen; however, the $SOCl_2$:$LiAlCl_4$ electrolyte is not
268 distinguishable from the liquid cathode. Regions which are filled with an excess of electrolyte

269 are expected in this cell type and can be seen above the active cell material by a reduction of

270 the electrolyte volume and an increase of the gas volume in the battery head during the

271 discharge. The lithium metal anode is indirectly visible by the transparent region at the outer

272 cell radius between cathode and the stainless steel cell can. The removal of lithium from the

273 electrode is indirectly detected during the discharge process. A contrast change inside the

274 $SOCl_2$ cathode is not detected. During the discharging process SO_2 gas is formed from the

275 reaction of lithium with $SOCl_2$ which is visible as bright purple areas due to a low attenuation

276 coefficient, which is similar to air. Shortly after the initiation of the discharge process, the SO_2

277 gas forms bubbles in the cathode which diffuse into four gas channels, which work as gas

278 guides in the porous carbon mesh, and accumulate inside the cell header where a further gas

279 reservoir is located. This transfer of SO_2 gas away from the cathode is designed to prevent the

280 stagnation of lithium diffusion and subsequent passivation of the anode surface during the

281 discharge. A distinction between the evolved SO_2 gas and the lithium metal is not possible in

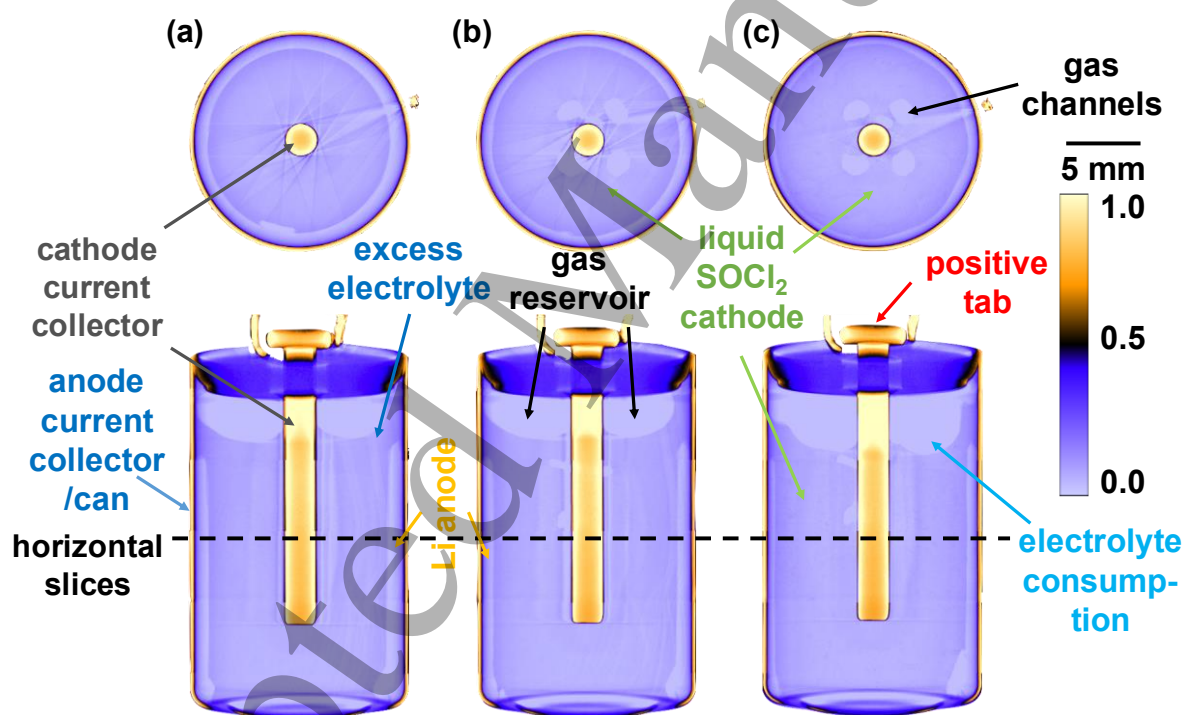282 the X-ray image, because the greyscale values cannot be sufficiently differentiated.

283

284 **Figure 3: Orthogonal slices from the 4D X-ray scan of the LS14250 battery cell discharged at 25 mA, showing horizontal and vertical**

285 **orthogonal slices from the in operando X-ray scan at three different SoCs; pristine, half discharged and the fully discharged cell.**

286 To provide a better understanding of the processes involved in the discharge of the cell,

287 including the removal of Li from the metal anode and the diffusion process inside the $SOCl_2$

288 cathode, complementary neutron imaging was used. Time resolved neutron tomography

289 mitigates the challenges associated with X-ray imaging discussed previously, and due to the

290 high sensitivity of neutrons to lithium, a quantitative description of the Li removal from the

291 anode and the diffusion of Li inside the thionyl chloride cathode can be achieved. Figure 4

292 shows orthogonal slices obtained on CONRAD-2 from the cell discharged at 25 mA: in pristine

293 condition, halfway through discharge and fully discharged, at which point the cell had delivered

294 a capacity of 506 mAh. In contrast to the X-ray tomographies, neutrons exhibit just a weak

295 attenuation by the metallic cell components such as the stainless steel container or the positive

296 battery tab. As seen in Figure 4, the Ni, cathode current collector exhibits a similar neutron

297 attenuation to the surrounding liquid $SOCl_2$ cathode and is difficult to distinguish. However, as

298 the Li content in the cathode increases, the current collector becomes more visible. More highly

299 attenuating cell components, such as the boron containing glass seal which shields the

300 environment from the toxic SO_2 gas and the Li, are shown in bright yellow colours. As

301 previously shown in the X-ray images (Figure 3), a contrast difference between the electrolyte

302 and the liquid cathode in the pristine state is not observed, however, as the discharge process

303 progresses the cathode can be clearly distinguished from the electrolyte due to the increase of

304 the attenuation coefficient indicated by the colour change from purple to black to yellow. The

305 volume reduction in the excess electrolyte in the battery header becomes visible as the

306 discharge progresses, exposing the 'flower' like shapes of the supporting porous carbon

307 skeleton alongside the four gas channels in the horizontal orthoslices. During the discharge

308 process, Li is progressively removed from the metal anode around the cathode and diffuses

309 through the separator membrane, (which is not visible due to insufficient spatial resolution),

310 into the cathode. Here, the attenuation coefficient increases steadily, seen by an increase in

311 contrast starting from the cathode border. As more Li moves into the cathode a high contrast

312 gradient from the cathode edge into the middle of the cell can be seen. This is indicative of a

313 slow lithium diffusion rate inside the cathode. At the same time, SO_2 gas, which is neutron

314 transparent, evolved through the discharge reaction and is marked through an increase of lowly

315 attenuating regions in Figure 4. Towards the edge of the cathode, a larger volume of gas is

316 generated due to the higher Li concentration in close proximity to the anode and consequent

317 increased reactivity in this region. Not all of this gas diffuses into the gas channels and fills the

318 gas reservoir, with a portion diffusing through the electrolyte and, in places, covering the

319 surface of the anode, highlighted by green boxes in the slices in Figure 4. Such 'gas shielded'

320 Li surface areas cannot participate in the chemical reaction. As a result of the slow lithium

321 mobility in the cathode and the shielding of fresh lithium from the anode by gas the cell

322 performance is inhibited through a reduction in both the cell capacity and operating potential.
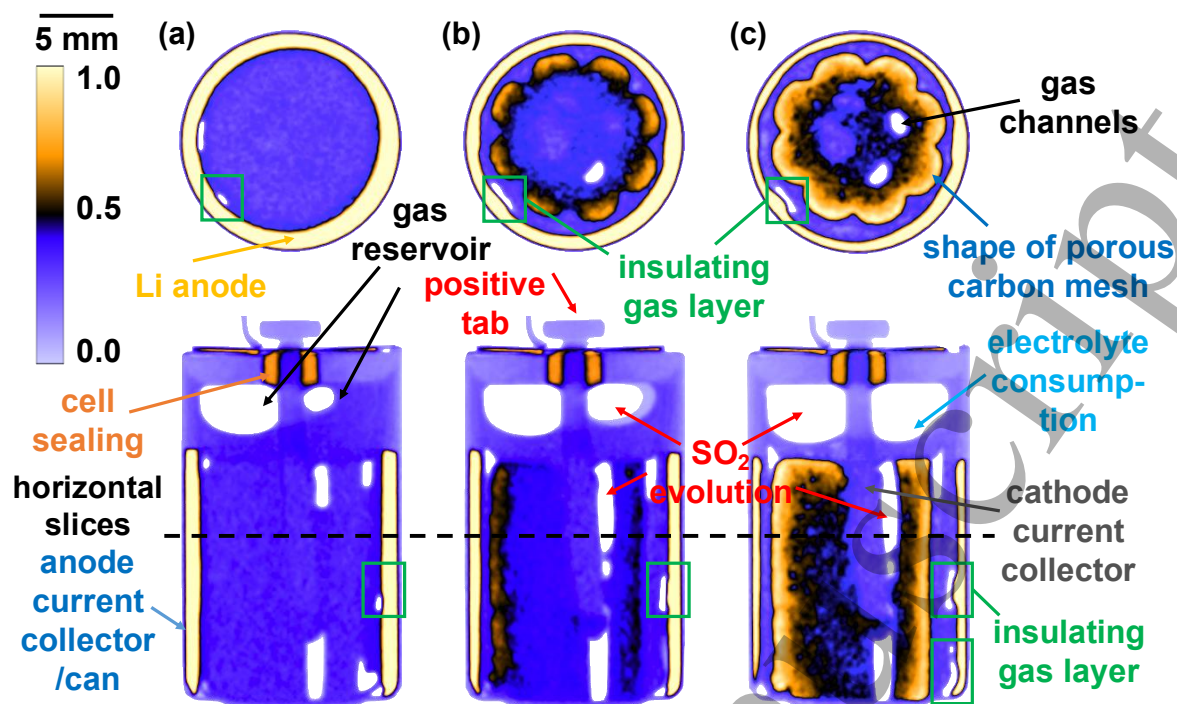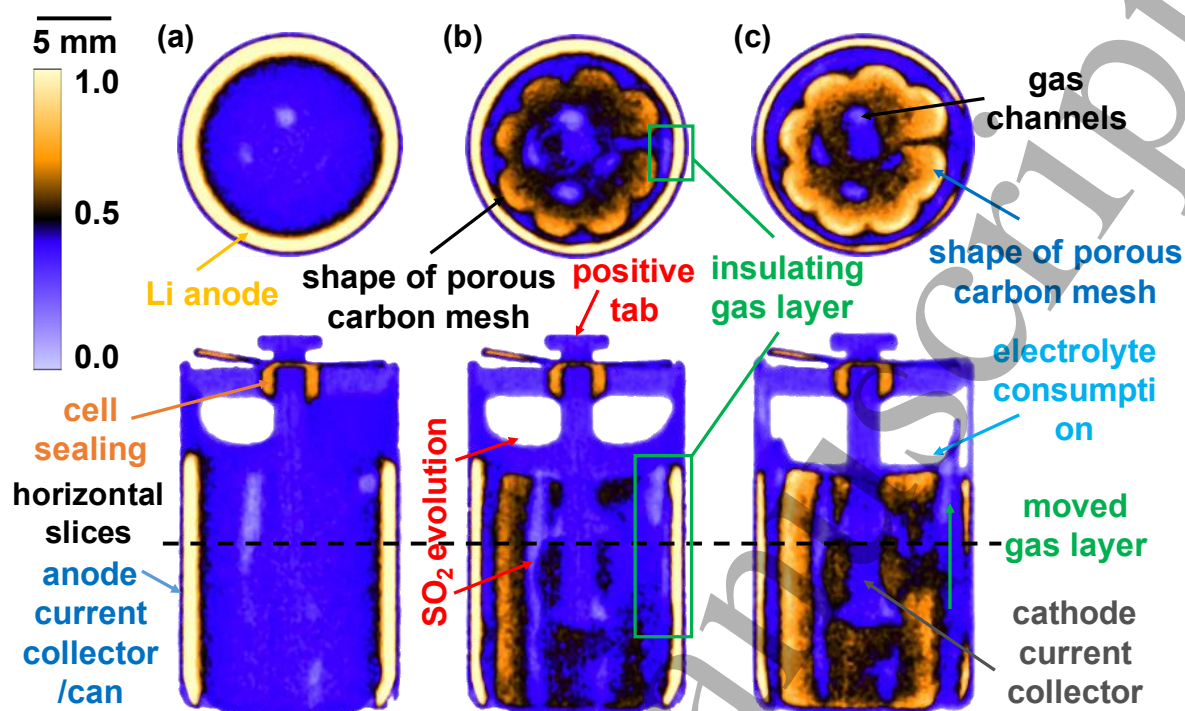
Figure 4: Orthogonal slices from the in-operando 3D neutron experiment of the LS14250 cell discharged at 25 mA at the CONRAD-2 neutron imaging beamline at three different SoCs: pristine, half discharged and fully discharged cell.

The second neutron imaging experiment provided data on a similar LS 14250 cell which was discharged at a lower discharge current of 8 mA. Orthogonal slices of three tomographies from IMAT are displayed in Figure 5, with slices from the pristine cell, in a half discharged condition and the fully discharged state with the cell yielding a total capacity of 832 mAh. The cell shows a similar discharge behaviour to that discharged at 25 mA, however, due to the lower discharge current the cell provided a ca. 40 % increase in capacity. This resulted in an increase in the consumption of lithium as seen in Figure 5, with the inhomogeneity of the lithium removal throughout the cell being particularly notable. The horizontal slices in Figure 5 initially show a homogeneous Li-metal anode in the pristine state and with the highly attenuating layer being preferentially removed towards the lower half and right hand side of the cell during discharge. This inhomogeneous Li consumption is likely caused by a misalignment of the cathode which is seen to be closer to the lower right anode side providing a shorter path to the cathode. Furthermore, evidence of the ability for gas to diffuse in this right hand region is shown in the tomograms with an area of gas evident at the surface of the anode observed when the cell is half-discharged not being present on full discharge. The lower discharge current used here also influences the quantity and depth of diffusion of Li in the cathode, which increases at lower operating currents due to the slow Li diffusion process in $SOCl_2$. This increased Li diffusion inside the cathode is likely the key reason for the improved cell capacity observed in this instance. At higher discharge currents, an increasing amount of lithium reacts in the outer

345 cathode region, forming insulating solid sulphur, which is deposited in the channels of the

346 porous carbon skeleton blocking the gas diffusion channels and ultimately insulating the

347 internal cathode where fresh $SOCl_2$ is available, thereby reducing the cell capacity.

348

Figure 5 Orthogonal slices from the in-operando 3D neutron experiment of the LS14250 cell discharged at 8 mA at the IMAT neutron imaging beamline at three different SoCs; pristine, half discharged and fully discharged cell.

351 By taking advantage of the high sensitivity of neutrons to Li shown previously, a quantitative

352 determination of the Li-anode volume over the discharge time is possible. Here, a constant

353 threshold segmentation of the bright lithium anode was achieved by using the AVIZO

354 visualisation software suite (Thermo Fisher Scientific, USA) with the results shown alongside

355 the discharge curves in Figure 6. In the case of the battery cell discharged at 25 mA, the 24

356 tomographies measured in the forward rotation direction were used for the segmentation. Three

357 of the segmented volumes are visualised in Figure 6(b). In the pristine state a total Li volume

358 of 615 mm^3 was measured with 356 mm^3 remaining after the discharge process was complete.

359 The anode shows a flat and homogeneous inner and outer surface area in the pristine state.

360 During the discharge process progressive lithium removal is clearly visible at the internal

361 electrode in the shape of vertical stripes. These stripes are located directly opposite the bulges

362 of the 'flower' shaped cathode seen in Figure 4 and Figure 5. The shorter distance between the

363 electrodes at these locations facilitates increased Li removal from the anode. The overlap of

364 the Li-metal at the left side of the segmented anode, caused by the manufacturing process, is

365 also visible with a shift in height between both endings.

366

367 While the initial Li volume of the cell discharged at 8 mA is similar (608 mm^3) the Li volume

368 change is more substantial, with 213 mm^3 remaining in the fully discharged state. Here, the Li

369 anode volume was determined for every second tomography. No overlap of the lithium metal

370 foil endings is visible which may be a result either of better initial fabrication or insufficient

371 spatial resolution. During the discharge process more lithium is consumed owing to the lower

372 discharge current, resulting in the complete removal of Li at one side of the anode.
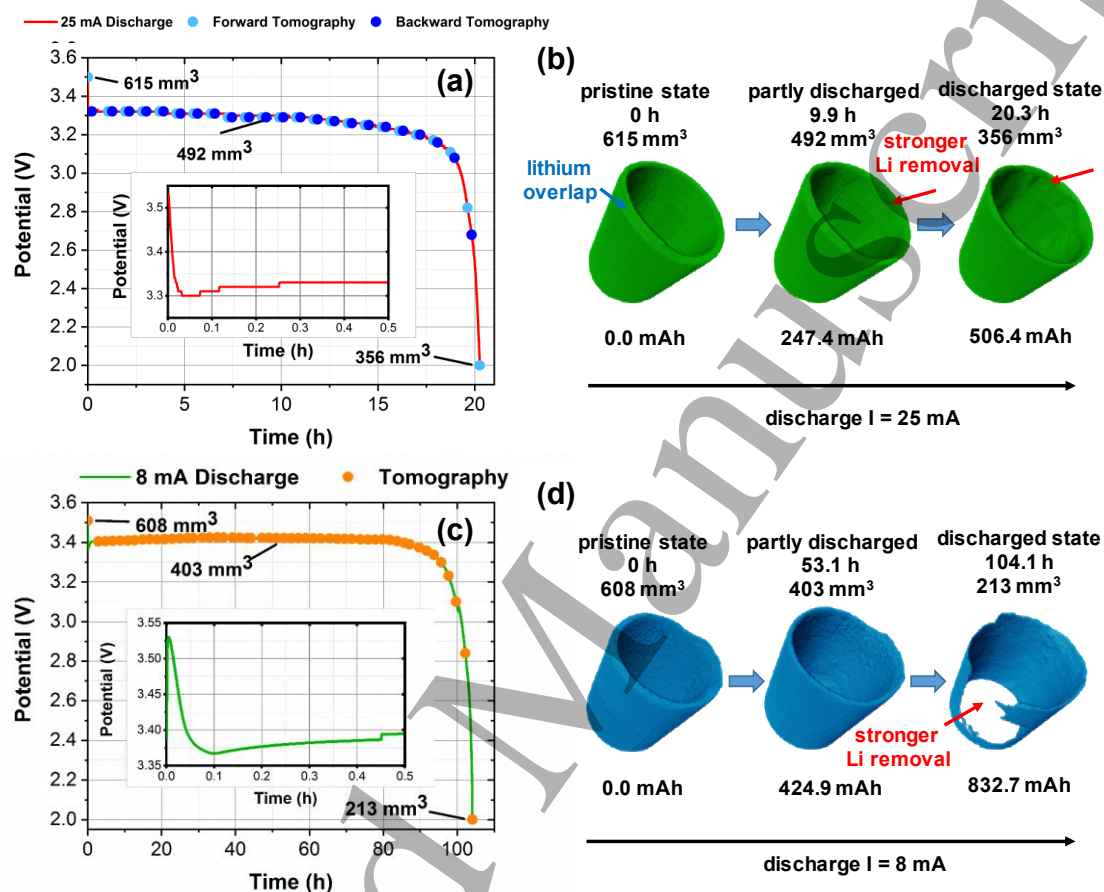

373

374 **Figure 6: Discharge curve of the LS14250 cell discharged at (a) 25 mA and (c) 8 mA alongside volume renderings of the anode volumes**

375 **of the cells discharged at (b) 25 mA and (d) 8 mA at different SoCs with the pristine, half and fully discharged state:**

376 Quantification of this Li volume decrease is achieved by correlating the volume of Li at a given

377 time to the capacity provided by the cell with this relationship following a linear trend as

378 observed in Figure 7. The initial Li metal volumes of 615 mm^3 and 608 mm^3, which correspond

379 to a Li mass of ca. 0.32 g per cell (based on a Li density at 20 °C of 0.534 g cm^{-3}), are in a good

380 agreement with the manufacturer's data sheet values of approximately 0.3 g per cell. The

381 theoretical relationship between the used Li volume in mm^3 and the resulting capacity delivered

382 in Ah is given in Equation 3. Here, M_{Li} corresponds to the molar mass of lithium, C the electric

383 charge, N_A the Avogadro constant and ρ_{Li} the density of lithium.

$$\left[\frac{mm^3}{Ah}\right] = \frac{M_{Li} \cdot 3600 \left[\frac{s}{h}\right]}{C \cdot N_A \cdot \rho_{Li}} = 485 \; \frac{mm^3}{Ah} \qquad\qquad \text{Equation 3}$$

384 It can be seen that a Li removal rate of 485 mm^3 Ah^{-1} is theoretically required for a Li/SOCl$_2$
385 cell which corresponds to a minimum initial Li volume of 582 mm^3, or mass of 0.31 g, for the
386 cells examined in this work. By comparing this to the measured volumes it can be seen that in
387 this case the significant majority of the anode must be consumed to deliver the rated 1.2 Ah
388 capacity. Experimentally determined Li removal rates can be calculated by interrogating the
389 slope of the curves shown in Figure 7. Here it is shown that 514 mm^3 Ah^{-1} and 462 mm^3 Ah^{-1}
390 are required for the cells discharged at 25 and 8 mA, respectively. The discrepancy between the
391 values for the two cells can be explained by different thresholds for the volume segmentation
392 arising from the different neutron spectra of CONRAD-2 and IMAT which result in different
393 average attenuation coefficients for Li. Further, a slightly different utilised threshold can affect
394 a deviation of several cubic millimetres as well as the relative big pixel sizes which can lead to
395 a slightly higher or lower determined lithium volume. To provide a more representative
396 comparison with this theoretical value it is beneficial to use the mean of 488 mm^3 Ah^{-1} of the
397 two measured values.
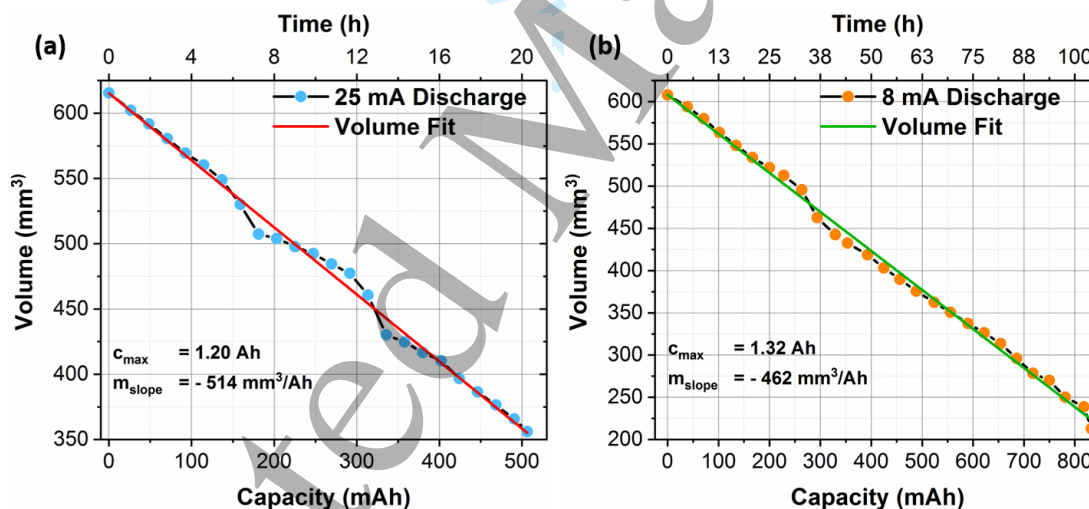
398

399 **Figure 7: Lithium volume decrease of the LS14250 anode during a discharge current of (a) 25 mA and (b) 8 mA, respectively. The**
400 **deviations from the expected linear volume reduction are due to variations in the segmentation process. The total error of the lithium**
401 **volume determination is estimated to be smaller than 5 %.**

402

403 A considerable drawback of the SOCl$_2$ electrode chemistry is the slow Li diffusion inside the
404 cathode which can result in blocking of the diffusion channels in the carbon support skeleton
405 by the formation of solid sulphur from the chemical reaction with lithium. Quantification of
406 this can be achieved by examining changes in intensity, which indicates the Li diffusion
407 throughout the cell. Figure 8(c, d) shows profiles of the intensity through the reconstructed

408 slices of the anode and cathode for both the cell discharged at 25 mA and 8 mA. For the line

409 profiles a single horizontal orthogonal slice was used, which is the most representative for the

410 battery cell respectively, shown in Figure 8(a, b). A high lithium mobility can be seen at the

411 cathode edges over the discharge time for both cells, with the 25 mA discharged cell showing

412 a higher mobility as a result of the increased discharge current [Figure 8(c, d)].
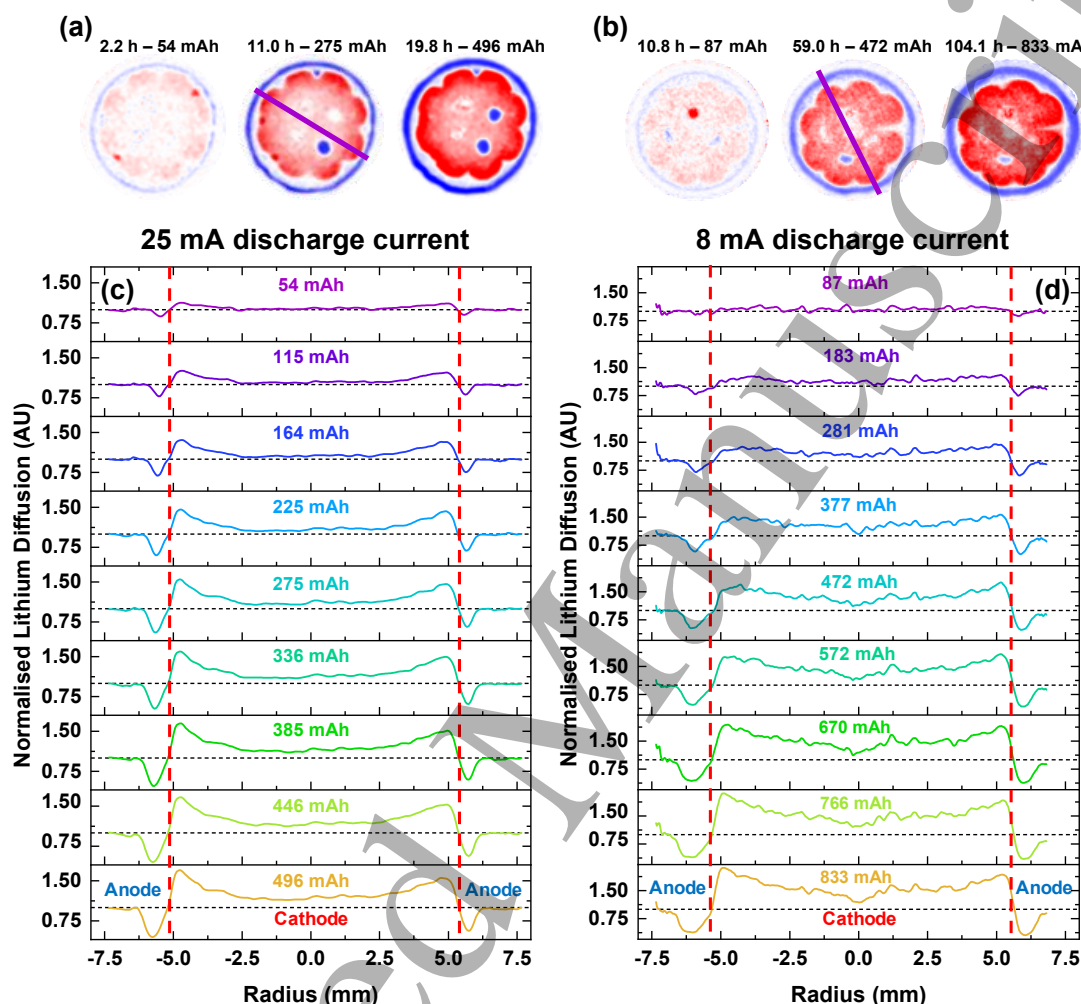
413

414 **Figure 8: Normalised grey values representing lithium redistributions inside the LS14250 battery cell during a discharge current of –**

415 **(a, c) 25 mA and (b, d) 8 mA. (a, b) selected horizontal slices from the middle part of the cell at different SoCs highlighting lithium**

416 **removal and accumulation. (c, d) time dependent line plots through the middle section of a LS14250 Li/SOCl$_2$ cell during the**

417 **discharging process. Values above the baseline indicate an increase of lithium in the cathode, and values below the baseline indicate**

418 **lithium removal from the anode.**

419 The x-axis shows the radial distance from the centre of the cell, and the y-axis the relative

420 change of the lithium distribution in terms of greyscale values normalised to the initial SoC.

421 Values above the baseline are attributable to an increased lithium content (such as that observed

422 in the SOCl$_2$ electrode), with reductions in intensity associated with a decrease of lithium

423 concentration (as seen in the lithium metal anode). The low lithium amount in the inner cathode

424 region, shown by a trough in intensity towards the centre of the cell indicates a substantial

425 stagnation in the lithium diffusion at a 25 mA discharge current. Figure 8(a) shows related
426 horizontal slices where blue and red colours indicate the lithium removal and deposition,
427 respectively. A high lithium accumulation at the bulges of the 'flower' shaped cathode
428 boundary is clearly visible during the first discharge phase due to the favourable short distance
429 between the lithium metal anode and the cathode. At the end of the discharging process, the
430 red ring along the cathode border indicates high accumulation of lithium in contrast to the inner
431 cathode region which is almost devoid of lithium. It should be noted that the blue coloured,
432 circular regions inside the cathode are related to intensity changes in the reconstructions caused
433 by the generation of SO_2 gas which fill the gas channels, displacing the $SOCl_2$ and causing a
434 similar behaviour to that observed during Li removal from the anode. White areas represent no
435 intensity changes during the discharging process which indicates regions with constant lithium
436 amounts or regions unaffected by the reaction.

437 Figure 8(b, d) shows a similar analysis for the cell discharged at 8 mA. In this case, the line
438 profile plot shows a more equal Li distribution from the outer cathode edge to the centre of the
439 cell. The lower discharge current facilitates improved Li diffusion properties due to the reduced
440 reaction rate. The improved ratio can be seen by the higher lithium amount in the centre of the
441 cathode in comparison to the cell discharged at 25 mA. The horizontal slices in Figure 8(b)
442 also show a more homogeneous lithium distribution during the discharge before the
443 concentration increases on the cathode border due to blocking effects in the carbon skeleton.
444 This comparison of the time dependent lithium distributions inside the $SOCl_2$ electrode reveals
445 the major reason for the capacity loss with discharge at higher currents. The loss of usable cell
446 capacity is strongly correlated to the rate of the lithium diffusion inside the cathode. Higher
447 currents force the chemical reaction between the Li and the thionyl chloride whereby solid
448 sulphur is formed impeding the diffusion channels of the porous supporting carbon skeleton
449 and reducing the rate of Li diffusion. As a consequence, fresh unreacted $SOCl_2$, stored in the
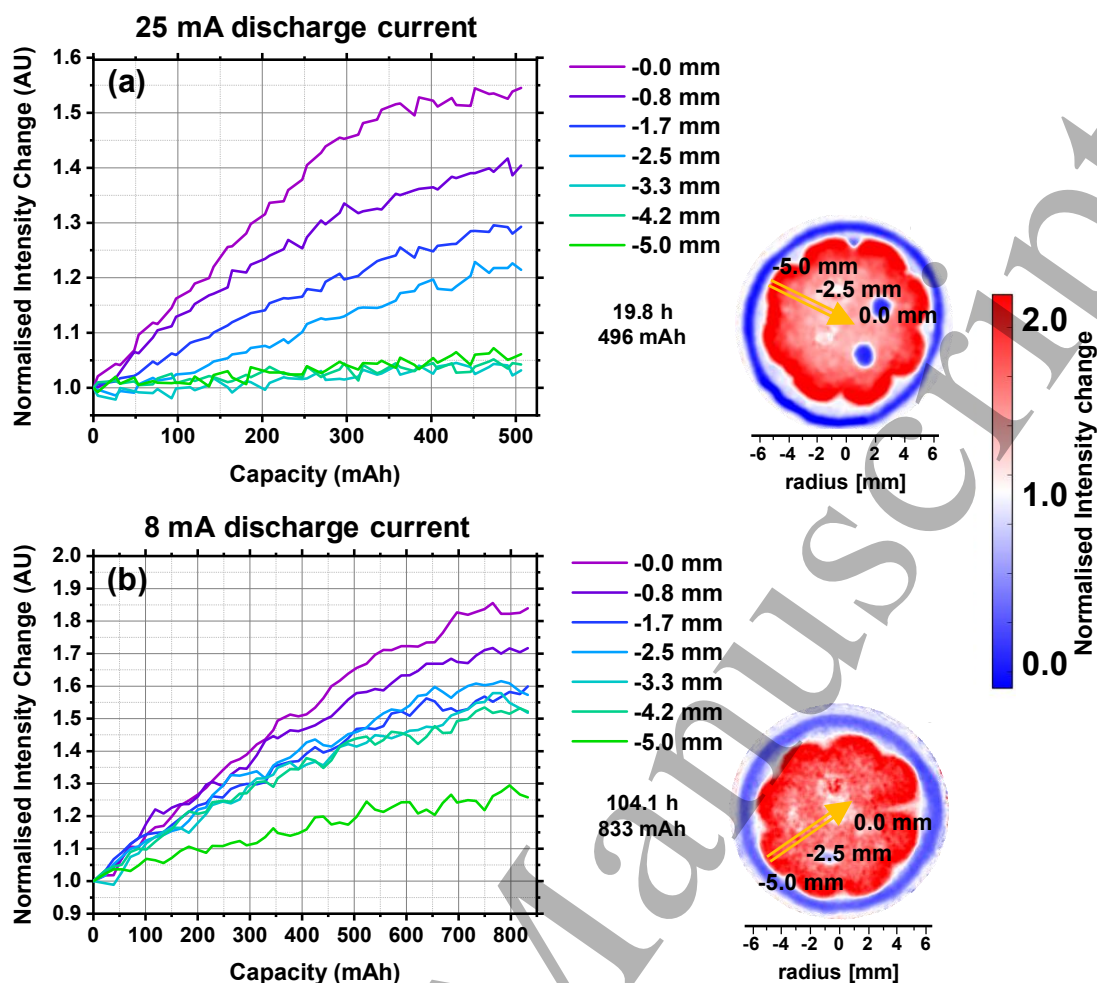450 inner cathode region, cannot participate in the reaction.

Figure 9: Relative grey value changes representing lithium diffusion inside the SOCl$_2$ cathode at (a) 25 mA and (b) 8 mA alongside horizontal slices from the middle of the cell, with the yellow arrow pointing along the selected analysis points.

To better understand the problem of capacity loss at higher discharge rates, an improved understanding of the lithium diffusion process in the cathode is necessary with results detailed in Figure 9 in which the time dependent normalised intensity change at seven different positions, starting at the cathode edge and evenly distributed regions along the arrow towards the centre, is measured in the most representative horizontal slices for both discharge rates. The detected normalised intensity can be interpreted as a measure of the quantity of Li present at any given position. Figure 9(a) presents the normalised intensity change from a radial distance of -5.0 to 0.0 mm for the cell discharged at 25 mA. The values were determined along a representative line which is shown in the orthoslice at different distances from the cathode centre. The line was placed in such a way that the gas channels do not influence the measurement result. The results shown in Figure 9(a) indicate an increased level of lithium at a radius of -5.0 mm, which steadily decreases through the cell to a boundary located at a radius of ca. -2.5 mm, beyond which no lithium is seen to diffuse. Above approximately 350 mAh, the lithium diffusion at the outer cathode part can be seen to plateau, indicating a saturation of the cathode. However,

468 due to the constant current discharge this stagnation of the Li diffusion must be compensated
469 by an increased rate of Li diffusion elsewhere. It is likely that this happens in the gaps between
470 the 'flowery' bulges at the cathode boundary, which are more active than other regions during
471 the initial part of discharge process owing to the shorter diffusion paths for the Li-ions from
472 anode to cathode. The rate of Li diffusion seems to only stagnate in the outer cathode region
473 (−5.0 mm) with an increase in intensity, and consequently continued diffusion, evident in the
474 inner regions (−4.2 mm to −2.5 mm) suggesting that the limitation on the capacity provided by
475 the cell occurs in the outer cathode shell area.

476 At a lower discharge current, the lithium diffusion inside the cathode is slightly more
477 homogeneous with a noticeable decrease inwards the cathode. Figure 9(b) shows the lithium
478 diffusion behaviour inside the $SOCl_2$ cathode for the cell discharged at 8 mA. In contrast to the
479 higher discharge current of 25 mA, the rate of intensity rise is consistent across all regions,
480 with the internal regions displaying a substantially increased change in intensity. These findings
481 demonstrate the mechanisms behind the improved capacity provided by lower operating
482 currents, which enables Li diffusion deeper inside the cathode enabling use of more unreacted
483 $SOCl_2$.
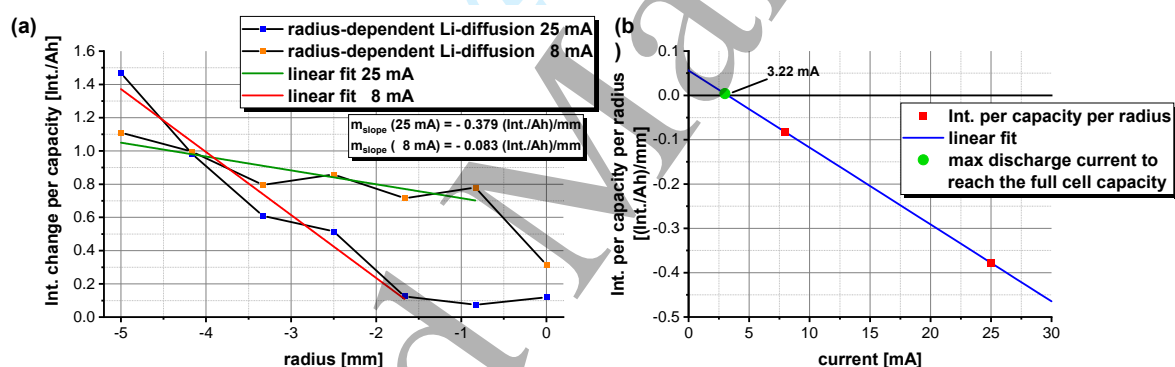
484

485 **Figure 10: Determination of the intensity/lithium amount change per cell capacity and the maximal discharge current which allows**
486 **for the use of the full cell capacity showing (a) the observed intensity change, and the calculated slopes for the cells discharged at**
487 **25 mA and 8 mA and (b) an estimation of the maximal usable discharge current to reach the full cell capacity occurring at the**
488 **intersection of the curve with the abscissa.**

489 The spatially variant intensity increase per capacity is a useful metric to compare the Li
490 diffusion behaviour inside the cathode for different discharge currents. The intensity-capacity
491 slopes for the graphs plotted in Figure 9 are displayed over the cathode radial distance in Figure
492 10. The slope values over the radial distance show a linear decrease of Li diffusion, with an
493 increased rate observed for the cell discharged at 25 mA scan due to higher Li use. At a radius
494 of about −1.5 mm the lithium diffusion seems to stop while the cell discharged at 8 mA shows
495 evidence of Li diffusion throughout the entire cell. The point shown at 0.0 mm includes a small
496 contribution in intensity of the cathode current collector which causes a slightly elevated

497 change. A fit of the slope of the linear region is a measure of the capacity and radius dependent

498 Li diffusion which is -0.379 (Int Ah^{-1}) mm^{-1} for the cell discharged at 25 mA and

499 -0.083 (Int Ah^{-1}) mm^{-1} for that at 8 mA. From the slope it is possible to determine a maximum

500 discharge current which enables the full capacity to be utilised. The Li diffusion per capacity

501 and radius is plotted over the discharge current in Figure 10 b). Assuming a linear dependence

502 for both values, the abscissa-axis intersection represents the maximal discharge current to reach

503 the full cell capacity and is marked with a green dot which corresponds to approximately 3.2

504 mA. This maximum cell utilisation rate is an order of magnitude lower than the maximum

505 recommended continuous current of 35 mA and demonstrates the capacity limitation

506 encountered at maximum discharge rate.

507

508 **Conclusions**

509 Multi-modal tomography was performed using X-rays and neutrons to elucidate the dynamic

510 processes which occur inside primary LiSOCl$_2$ cells during discharge. These complementary

511 methods enable the visualisation of the changes which occur in the cell components due to the

512 different attenuation characteristics in the two techniques. X-ray tomography identified the

513 consumption of the SOCl$_2$ electrolyte, which resulted in the evolution of SO$_2$ gas; however no

514 significant structural deformations were observed using this method. In contrast, neutron

515 imaging enabled the identification of the rate dependent diffusion characteristics of Li within

516 the cell. Time dependent neutron tomography was enabled through the use of the golden ratio

517 imaging technique, which substantially improves the temporal resolution of the imaging

518 process, even at low flux neutron sources. The gas evolved during discharge was found to

519 inhibit the performance by isolating regions of Li. Furthermore, the rate of Li diffusion was

520 observed to be spatially variable, with regions identified where the diffusion process was seen

521 to stagnate during discharge.

522

523 The two imaging methods have provided an improved understanding of the performance of the

524 cells. Where X-rays are more sensitive to metallic cell components such as the battery casing

525 or the current collectors, neutrons visualise inter alia the lithium diffusion. The combination of

526 both techniques helps to understand processes which are hidden for one technique or localise

527 battery components, such as the cathode current collector in the cell centre, which are invisible

528 for neutrons but the location is important for the analysis. For the discharge currents used in

529 this study, the capacity of the cells was observed to fall significantly short of the nominal

530 capacity, due to the slow lithium diffusion and the presence of unusable lithium. This bobbin

531 type cell design shows significant radial disparity in the rate of Li diffusion at higher discharge

532 rates suggesting a need to either limit the maximum current drawn from the cell or amend the

533 cell design to promote improved Li diffusion. A calculation to determine the maximum capacity

534 with this cell design suggests that the discharge rate (to ensure maximum capacity) should be
535 at least an order of magnitude lower than the maximum current suggested by the manufacturer.
536
537

538 **Acknowledgments**

546
547

548 **References**

549 [1] D.C. Bock, A.C. Marschilok, K.J. Takeuchi, E.S. Takeuchi, Batteries used to power
550   implantable biomedical devices, Electrochim. Acta. 84 (2012) 155–164.
551   https://doi.org/10.1016/j.electacta.2012.03.057.
552 [2] W. Chen, J. Liang, Z. Yang, G. Li, A review of lithium-ion battery for electric vehicle
553   applications and beyond, Energy Procedia. 158 (2019) 4363–4368.
554   https://doi.org/10.1016/j.egypro.2019.01.783.
555 [3] Y. Borthomieu, Satellite Lithium-Ion Batteries, Elsevier, 2014.
556   https://doi.org/10.1016/B978-0-444-59513-3.00014-5.
557 [4] R. Gangadharan, C. Electrochemical, P.N.N. Namboodiri, K. V Prasad, R. Viswanathan,
558   THE LITHIUM-THIONYL CHLORIDE BATTERY - A REVIEW, 4 (1979) 1–9.
559 [5] A.J. Hills, N.A. Hampson, The LiSOCl2 cell - a review, J. Power Sources. 24 (1988)
560   253–271. https://doi.org/10.1016/0378-7753(88)80102-2.
561 [6] J.J. Auborn, K.W. French, S.I. Lieberman, V.K. Shah, A. Heller, Lithium Anode Cells
562   Operating at Room Temperature in Inorganic Electrolytic Solutions, J. Electrochem. Soc.
563   120 (1973) 1613. https://doi.org/10.1149/1.2403315.
564 [7] W.K. Behl, J. a. Christopulos, M. Ramirez, S. Gilman, Lithium Inorganic Electrolyte
565   Cells Utilizing Solvent Reduction, J. Electrochem. Soc. 120 (1973) 1619.
566   https://doi.org/10.1149/1.2403316.
567 [8] M. Babai, M. Pallivathikal, Comparison of the behavior of the Li/SOCl2 and Ca/SOCl2
568   systems at elevated temperatures, J. Power Sources. 28 (1989) 325–334.
569   https://doi.org/10.1016/0378-7753(89)80062-X.
570 [9] C.R. Schlaikjer, F. Goebel, N. Marincic, Discharge Reaction Mechanisms in Li / SOCl2
571   Cells, J. Electrochem. Soc. 126 (1979) 513–522. https://doi.org/10.1149/1.2128899.
572 [10] P.R. Shearing, N.P. Brandon, J. Gelb, R. Bradley, P.J. Withers, A.J. Marquis, S. Cooper,
573   S.J. Harris, Multi Length Scale Microstructural Investigations of a Commercially
574   Available Li-Ion Battery Electrode, J. Electrochem. Soc. 159 (2012) A1023–A1027.
575   https://doi.org/10.1149/2.053207jes.

576 [11] D.P. Finegan, E. Darcy, M. Keyser, B. Tjaden, T.M.M. Heenan, R. Jervis, J.J. Bailey, R.
577   Malik, N.T. Vo, O. V. Magdysyuk, R. Atwood, M. Drakopoulos, M. DiMichiel, A. Rack,
578   G. Hinds, D.J.L. Brett, P.R. Shearing, Characterising thermal runaway within lithium-
579   ion cells by inducing and monitoring internal short circuits, Energy Environ. Sci. 10
580   (2017) 1377–1388. https://doi.org/10.1039/C7EE00385D.

581 [12] D.P. Finegan, B. Tjaden, T. M. M. Heenan, R. Jervis, M. Di Michiel, A. Rack, G. Hinds,
582   D.J.L. Brett, P.R. Shearing, Tracking Internal Temperature and Structural Dynamics
583   during Nail Penetration of Lithium-Ion Cells, J. Electrochem. Soc. 164 (2017) A3285–
584   A3291. https://doi.org/10.1149/2.1501713jes.

585 [13] D.P. Finegan, M. Scheel, J.B. Robinson, B. Tjaden, I. Hunt, T.J. Mason, J. Millichamp,
586   M. Di Michiel, G.J. Offer, G. Hinds, D.J.L. Brett, P.R. Shearing, In-operando high-speed
587   tomography of lithium-ion batteries during thermal runaway, Nat. Commun. 6 (2015)
588   1–10. https://doi.org/10.1038/ncomms7924.

589 [14] D.P. Finegan, M. Scheel, J.B. Robinson, B. Tjaden, M. Di Michiel, G. Hinds, D.J.L.
590   Brett, P.R. Shearing, Investigating lithium-ion battery materials during overcharge-
591   induced thermal runaway: an operando and multi-scale X-ray CT study, Phys. Chem.
592   Chem. Phys. 18 (2016) 30912–30919. https://doi.org/10.1039/C6CP04251A.

593 [15] D.P. Finegan, E. Tudisco, M. Scheel, J.B. Robinson, O.O. Taiwo, D.S. Eastwood, P.D.
594   Lee, M. Di Michiel, B. Bay, S.A. Hall, G. Hinds, D.J.L. Brett, P.R. Shearing, Quantifying
595   Bulk Electrode Strain and Material Displacement within Lithium Batteries via High-
596   Speed Operando Tomography and Digital Volume Correlation, Adv. Sci. 3 (2016)
597   1500332. https://doi.org/10.1002/advs.201500332.

598 [16] L. Zielke, T. Hutzenlaub, D.R. Wheeler, I. Manke, T. Arlt, N. Paust, R. Zengerle, S.
599   Thiele, A combination of X-ray tomography and carbon binder modeling:
600   Reconstructing the three phases of LiCoO2 Li-ion battery cathodes, Adv. Energy Mater.
601   4 (2014) 2–7. https://doi.org/10.1002/aenm.201301617.

602 [17] A.G. Kashkooli, S. Farhad, D.U. Lee, K. Feng, S. Litster, S.K. Babu, L. Zhu, Z. Chen,
603   Multiscale modeling of lithium-ion battery electrodes based on nano-scale X-ray
604   computed tomography, J. Power Sources. 307 (2016) 496–509.
605   https://doi.org/10.1016/j.jpowsour.2015.12.134.

606 [18] S.R. Daemi, C. Tan, T. Volkenandt, S.J. Cooper, A. Palacios-Padros, J. Cookson, D.J.L.
607   Brett, P.R. Shearing, Visualizing the Carbon Binder Phase of Battery Electrodes in Three
608   Dimensions, ACS Appl. Energy Mater. 1 (2018) 3702–3710.
609   https://doi.org/10.1021/acsaem.8b00501.

610 [19] P. Boillat, E.H. Lehmann, P. Trtik, M. Cochet, Neutron imaging of fuel cells – Recent
611   trends and future prospects, Curr. Opin. Electrochem. 5 (2017) 3–10.
612   https://doi.org/10.1016/j.coelec.2017.07.012.

613 [20] P. Oberholzer, P. Boillat, Local Characterization of PEFCs by Differential Cells:
614   Systematic Variations of Current and Asymmetric Relative Humidity, J. Electrochem.
615   Soc. 161 (2014) F139–F152. https://doi.org/10.1149/2.080401jes.

616 [21] Y. Wu, Q. Meyer, F. Liu, L. Rasha, J.I.S. Cho, T.P. Neville, J. Millichamp, R. Ziesche,
617   N. Kardjilov, P. Boillat, H. Markötter, I. Manke, M. Cochet, P. Shearing, D.J.L. Brett,

618 Investigation of water generation and accumulation in polymer electrolyte fuel cells
619 using hydro-electrochemical impedance imaging, J. Power Sources. 414 (2019) 272–
620 277. https://doi.org/10.1016/j.jpowsour.2019.01.003.

621 [22] M. Maier, J. Dodwell, R. Ziesche, C. Tan, T. Heenan, J. Majasan, N. Kardjilov, H.
622 Markötter, I. Manke, L. Castanheira, G. Hinds, P.R. Shearing, D.J.L. Brett, Mass
623 transport in polymer electrolyte membrane water electrolyser liquid-gas diffusion layers:
624 A combined neutron imaging and X-ray computed tomography study, J. Power Sources.
625 455 (2020). https://doi.org/10.1016/j.jpowsour.2020.227968.

626 [23] C.H. Lee, R. Banerjee, N. Ge, J.K. Lee, B. Zhao, E. Baltic, J.M. LaManna, D.S. Hussey,
627 D.L. Jacobson, R. Abouatallah, R. Wang, A. Bazylak, The effect of cathode nitrogen
628 purging on cell performance and in operando neutron imaging of a polymer electrolyte
629 membrane electrolyzer, Electrochim. Acta. 279 (2018) 91–98.
630 https://doi.org/10.1016/j.electacta.2018.05.066.

631 [24] J.B. Siegel, X. Lin, A.G. Stefanopoulou, D.S. Hussey, D.L. Jacobson, D. Gorsich,
632 Neutron Imaging of Lithium Concentration in LFP Pouch Cell Battery, J. Electrochem.
633 Soc. 158 (2011) A523–A529. https://doi.org/10.1149/1.3566341.

634 [25] J.B. Siegel, A.G. Stefanopoulou, P. Hagans, Y. Ding, D. Gorsich, Expansion of Lithium
635 Ion Pouch Cell Batteries: Observations from Neutron Imaging, J. Electrochem. Soc. 160
636 (2013) A1031–A1038. https://doi.org/10.1149/2.011308jes.

637 [26] H. Zhou, K. An, S. Allu, S. Pannala, J. Li, H.Z. Bilheux, S.K. Martha, J. Nanda, Probing
638 Multiscale Transport and Inhomogeneity in a Lithium-Ion Pouch Cell Using In Situ
639 Neutron Methods, ACS Energy Lett. 1 (2016) 981–986.
640 https://doi.org/10.1021/acsenergylett.6b00353.

641 [27] G. V. Riley, D.S. Hussey, D.L. Jacobson, In Situ Neutron Imaging of Alkaline and
642 Lithium-Ion Batteries, ECS Trans. 25 (2010) 75–83.

643 [28] M. Lanz, E. Lehmann, R. Imhof, I. Exnar, P. Novák, In situ neutron radiography of
644 lithium-ion batteries during charge/discharge cycling, J. Power Sources. 101 (2001)
645 177–181. https://doi.org/10.1016/S0378-7753(01)00706-6.

646 [29] B. Michalak, H. Sommer, D. Mannes, A. Kaestner, T. Brezesinski, J. Janek, Gas
647 Evolution in Operating Lithium-Ion Batteries Studied In Situ by Neutron Imaging, Sci.
648 Rep. 5 (2015) 1–9. https://doi.org/10.1038/srep15627.

649 [30] B. Michalak, B.B. Berkes, H. Sommer, T. Bergfeldt, T. Brezesinski, J. Janek, Gas
650 Evolution in LiNi0.5Mn1.5O4/Graphite Cells Studied In Operando by a Combination
651 of Differential Electrochemical Mass Spectrometry, Neutron Imaging, and Pressure
652 Measurements, Anal. Chem. 88 (2016) 2877–2883.
653 https://doi.org/10.1021/acs.analchem.5b04696.

654 [31] D. Goers, M. Holzapfel, W. Scheifele, E. Lehmann, P. Vontobel, P. Novák, In situ
655 neutron radiography of lithium-ion batteries: The gas evolution on graphite electrodes
656 during the charging, J. Power Sources. 130 (2004) 221–226.
657 https://doi.org/10.1016/j.jpowsour.2003.11.065.

658 [32] C. Tötzke, N. Kardjilov, I. Manke, S.E. Oswald, Capturing 3D Water Flow in Rooted
659 Soil by Ultra-fast Neutron Tomography, Sci. Rep. 7 (2017) 6192.

660   https://doi.org/10.1038/s41598-017-06046-w.

661 [33] C. Tötzke, N. Kardjilov, N. Lenoir, I. Manke, S.E. Oswald, A. Tengattini, What comes
662   NeXT? – High-Speed Neutron Tomography at ILL, 27 (2019) 28640–28648.
663   https://doi.org/10.1364/OE.27.028640.

664 [34] A. Tengattini, N. Lenoir, E. Andò, B. Giroud, D. Atkins, J. Beaucour, G. Viggiani,
665   NeXT-Grenoble, the Neutron and X-ray tomograph in Grenoble, Nucl. Instruments
666   Methods Phys. Res. Sect. A Accel. Spectrometers, Detect. Assoc. Equip. 968 (2020) 1–
667   11. https://doi.org/10.1016/j.nima.2020.163939.

668 [35] D.S. Hussey, J.M. LaManna, E. Baltic, D.L. Jacobson, Neutron imaging detector with 2
669   μm spatial resolution based on event reconstruction of neutron capture in gadolinium
670   oxysulfide scintillators, Nucl. Instruments Methods Phys. Res. Sect. A Accel.
671   Spectrometers, Detect. Assoc. Equip. 866 (2017) 9–12.
672   https://doi.org/10.1016/j.nima.2017.05.035.

673 [36] P. Trtik, J. Hovind, C. Grünzweig, A. Bollhalder, V. Thominet, C. David, A. Kaestner,
674   E.H. Lehmann, Improving the Spatial Resolution of Neutron Imaging at Paul Scherrer
675   Institut - The Neutron Microscope Project, Phys. Procedia. 69 (2015) 169–176.
676   https://doi.org/10.1016/j.phpro.2015.07.024.

677 [37] A. Kaestner, B. Münch, P. Trtik, L. Butler, Spatiotemporal computed tomography of
678   dynamic processes, Opt. Eng. 50 (2011) 123201. https://doi.org/10.1117/1.3660298.

679 [38] T. Kohler, A projection access scheme for iterative reconstruction based on the golden
680   section, Nucl. Sci. Symp. Conf. Rec. 2004 IEEE. 6 (2004) 3961-3965 Vol. 6.
681   https://doi.org/10.1109/NSSMIC.2004.1466745.

682 [39] J.M. LaManna, D.S. Hussey, E.M. Baltic, D.L. Jacobson, Improving material
683   identification by combining x-ray and neutron tomography, Proc. SPIE. 1039104 (2017)
684   1–7. https://doi.org/10.1117/12.2274443.

685 [40] R.F. Ziesche, T. Arlt, D.P. Finegan, T.M.M. Heenan, A. Tengattini, D. Baum, N.
686   Kardjilov, H. Markötter, I. Manke, W. Kockelmann, D.J.L. Brett, P.R. Shearing, 4D
687   imaging of lithium-batteries using correlative neutron and X-ray tomography with a
688   virtual unrolling technique, Nat. Commun. 11:777 (2020) 11.
689   https://doi.org/10.1038/s41467-019-13943-3.

690 [41] SAFT, Data Sheet - SAFT LS 14250, (2009) 1–2.

691 [42] N. Kardjilov, A. Hilger, I. Manke, R. Woracek, J. Banhart, CONRAD-2: The new
692   neutron imaging instrument at the Helmholtz-Zentrum Berlin, J. Appl. Crystallogr. 49
693   (2016) 195–202. https://doi.org/10.1107/S1600576715023353.

694 [43] N. Kardjilov, A. Hilger, I. Manke, CONRAD-2: Cold Neutron Tomography and
695   Radiography at BER II (V7), J. Large-Scale Res. Facil. JLSRF. 2 (2016) 1–6.
696   https://doi.org/10.17815/jlsrf-2-108.

697 [44] J. Schindelin, I. Arganda-carreras, E. Frise, V. Kaynig, M. Longair, T. Pietzsch, S.
698   Preibisch, C. Rueden, S. Saalfeld, B. Schmid, J. Tinevez, D.J. White, V. Hartenstein, K.
699   Eliceiri, P. Tomancak, A. Cardona, Fiji : an open-source platform for biological-image
700   analysis, Nat. Methods. 9 (2012) 676–682. https://doi.org/10.1038/nmeth.2019.

701 [45] W. Kockelmann, T. Minniti, D. Pooley, G. Burca, R. Ramadhan, F. Akeroyd, G. Howells,

702   C. Moreton-Smith, D. Keymer, J. Kelleher, S. Kabra, T. Lee, R. Ziesche, A. Reid, G.
703   Vitucci, G. Gorini, D. Micieli, R. Agostino, V. Formoso, F. Aliotta, R. Ponterio, S.
704   Trusso, G. Salvato, C. Vasi, F. Grazzi, K. Watanabe, J. Lee, A. Tremsin, J. McPhate, D.
705   Nixon, N. Draper, W. Halcrow, J. Nightingale, Time-of-Flight Neutron Imaging on
706   IMAT@ISIS: A New User Facility for Materials Science, J. Imaging. 4 (2018) 47.
707   https://doi.org/10.3390/jimaging4030047.

708   [46]   T. Minniti, W. Kockelmann, G. Burca, J.F. Kelleher, S. Kabra, S.Y. Zhang, D.E. Pooley,
709   E.M. Schooneveld, Q. Mutamba, J. Sykora, N.J. Rhodes, F.M. Pouzols, J.B. Nightingale,
710   F. Aliotta, L.M. Bonaccorsi, R. Ponterio, G. Salvato, S. Trusso, C. Vasi, A.S. Tremsin,
711   G. Gorini, Materials analysis opportunities on the new neutron imaging facility
712   IMAT@ISIS, J. Instrum. 11 (2016) C03014–C03014. https://doi.org/10.1088/1748-
713   0221/11/03/C03014.

714   [47]   T. Minniti, K. Watanabe, G. Burca, D.E. Pooley, W. Kockelmann, Characterization of
715   the new neutron imaging and materials science facility IMAT, Nucl. Instruments
716   Methods Phys. Res. 888 (2017) 184–195. https://doi.org/10.1016/j.nima.2018.01.037.

717   [48]   W. van Aarle, W.J. Palenstijn, J. Cant, E. Janssens, F. Bleichrodt, A. Dabravolski, J. De
718   Beenhouwer, K. Joost Batenburg, J. Sijbers, Fast and flexible X-ray tomography using
719   the ASTRA toolbox, Opt. Express. 24 (2016) 25129.
720   https://doi.org/10.1364/OE.24.025129.

721   [49]   W. van Aarle, W.J. Palenstijn, J. De Beenhouwer, T. Altantzis, S. Bals, K.J. Batenburg,
722   J. Sijbers, The ASTRA Toolbox: A platform for advanced algorithm development in
723   electron tomography, Ultramicroscopy. 157 (2015) 35–47.
724   https://doi.org/10.1016/j.ultramic.2015.05.002.

725   [50]   A.N. Dey, S.E.M. studies of the Li-film growth and the voltage-delay phenomenon
726   associated with the lithium-thionyl chloride inorganic electrolyte system, Electrochim.
727   Acta. 21 (1976) 377–382. https://doi.org/10.1016/0013-4686(76)85029-3.

728